



Cite this: *Nanoscale*, 2015, 7, 6827

## Transformation of truncated gold octahedrons into triangular nanoprisms through the heterogeneous nucleation of silver†

K. D. Gilroy,<sup>‡a</sup> A. Sundar,<sup>‡a</sup> M. Hajfathalian,<sup>a</sup> A. Yaghoubzade,<sup>a</sup> T. Tan,<sup>b</sup> D. Sil,<sup>c</sup> E. Borguet,<sup>c</sup> R. A. Hughes<sup>a</sup> and S. Neretina<sup>\*a</sup>

Described is a straightforward procedure for forming organized substrate-immobilized nanoprisms which are single crystalline, surfactant-free and which form a heteroepitaxial relationship with the underlying substrate. The devised route utilizes truncated Au octahedrons formed through solid state dewetting techniques as high temperature heterogeneous nucleation sites for Ag adatoms which are arriving to the substrate surface in the vapour phase. Observed is a morphological and compositional transformation of the Au structures to triangular nanoprisms comprised of a homogeneous AuAg alloy. During this transformation, the localized surface plasmon resonance red-shifts, broadens and increases in strength. The shape transformation, which cannot be rationalized using thermodynamic arguments dependent on the surface energy minimization, is described in terms of a kinetically driven growth mode, previously predicted by molecular dynamic simulations. The so-formed structures, when coated with a thin layer of Pd, are demonstrated as plasmonic sensing elements for hydrogen detection.

Received 8th January 2015,  
Accepted 17th March 2015

DOI: 10.1039/c5nr00151j

www.rsc.org/nanoscale

### Introduction

Photonic surfaces comprised of substrate-immobilized noble metal nanostructures provide the means to advance numerous catalytic,<sup>1,2</sup> photovoltaic<sup>3–6</sup> and sensing applications.<sup>7–10</sup> Nanostructures with shape anisotropies, such as nanorods<sup>11</sup> and triangular nanoprisms,<sup>12</sup> are particularly attractive to such applications due to the high tunability of the plasmon resonance. Nanoprisms are further valued for the intense plasmonic near-fields formed at the triangle tips,<sup>13</sup> a response which can be further amplified by placing two such structures in close proximity in a bow tie configuration.<sup>14</sup> There is also growing interest in the use of these structures as templates capable of defining more intricate nanostructure geometries.<sup>15,16</sup> Mirkin and co-workers, using a solution-based photochemical synthesis, were the first to synthesize triangular nanoprisms in high yield.<sup>17</sup> The discovery spurred on considerable interest and activity which has recently given rise to the emergence of seed-mediated protocols offering higher yields, greater

monodispersity, an increased size range and synthetic simplicity.<sup>18–20</sup>

Even though solution-based routes have proven extremely successful in the synthesis of noble metal nanoprisms, many of the aforementioned applications require that such structures be placed on substrate surfaces. While the dispersal of these nanoprisms onto planar substrates is relatively straightforward, it results in structures which are positioned randomly on the surface<sup>21</sup> or which form an uncontrolled self-assembled pattern.<sup>18</sup> Lithographic techniques have been used to define nanoprisms at site-specific locations,<sup>22–24</sup> but these approaches can have limitations associated with long processing times, high cost and the low quality factors associated with the LSPR of polycrystalline structures.<sup>25,26</sup> Recognizing the benefits of placing single crystal nanoprisms onto a substrate surface in an organized manner, Zhou *et al.*<sup>27</sup> lithographically defined triangular trenches into a substrate which were able to accept nanoprisms dispersed in an evaporating droplet. While impressive, the surfaces of these structures remain coated with capping agents which can negatively impact nanostructure properties.<sup>28,29</sup> Fabricating periodic arrays of noble metal nanoprisms which are surfactant-free, substrate-immobilized, and single crystalline is, therefore, a synthetic challenge which has not previously been met.

Physical vapour deposition (PVD) or assembly routes based on solid state dewetting, when carried out on substrates which support an epitaxial relationship, all allow for island growth

<sup>a</sup>College of Engineering, Temple University, Philadelphia, Pennsylvania 19122, USA.  
E-mail: neretina@temple.edu

<sup>b</sup>Physics Department, Temple University, Philadelphia, Pennsylvania 19122, USA

<sup>c</sup>Chemistry Department, Temple University, Philadelphia, Pennsylvania 19122, USA

†Electronic supplementary information (ESI) available. See DOI: 10.1039/c5nr00151j

‡These authors contributed to this work equally.

modes yielding single crystalline nanostructures.<sup>30,31</sup> While forming [111]-oriented noble metal nanostructures is relatively straightforward using these techniques, the structures formed do not typically take on the nanoprism geometry. This is a consequence of the fact that island formation is reliant on high temperature solid state diffusion processes which support the formation of nanostructure geometries with low surface energies realised through a combination of minimizing the surface-to-volume ratio and forming low surface energy facets. Taking these factors into account for elements with face centered cubic (fcc) crystal structures (*e.g.* Au, Ag) leads to the equilibrium Wulff shape which is a truncated octahedron with eight hexagonal {111} facets and six square {100} facets.<sup>32</sup> While the exact nature of the epitaxial relationship between the forming nanostructure and the substrate can result in deviations from the Wulff geometry,<sup>30</sup> a substrate capable of promoting Au or Ag nanoprism formation in high yield has not yet been discovered.

Previously, we demonstrated the utility of using substrate-immobilized Au nanostructures as templates capable of directing high temperature assembly.<sup>33–35</sup> In these processes, Au nanostructures are confined between an oxide substrate and a second material from which adatoms can be sourced through sublimation. At the assembly temperature these adatoms are unable to spontaneously form stable clusters on the substrate surface. When they encounter a Au template, however, they are readily incorporated to form a new nanostructure with its own unique properties. This strategy has been demonstrated for scenarios where Au is transformed into an alloy,<sup>34,35</sup> where it forms a eutectic liquid which upon cooling phase separates into a heterodimer structure<sup>33</sup> and where the Au template is sacrificed and replaced with a Wulff-shaped Pd nanostructure.<sup>34</sup> Here, we demonstrate that an analogous strategy can be used to transform Wulff-shaped Au nanostructures into triangular AuAg nanoprisms. The transformation is explained in terms of anisotropic kinetic processes which continuously drive the structure towards a non-equilibrium geometry until the assembly process is terminated through cooling. The optical properties of the nanostructures and the hydrogen sensing capabilities of Pd covered nanoprisms are also reported.

## Results and discussion

### Synthesis of AuAg nanoprisms

Fig. 1a shows a schematic of the procedure used to transform substrate-immobilized Au templates into AuAg nanoprisms. The templates were prepared on (0001)-oriented sapphire substrates as both periodic arrays with a narrow size distribution and as randomly positioned structures with a broad size distribution.

The arrays were fabricated using dynamic templating, a lithography-free templated assembly technique which we describe in detail elsewhere,<sup>36</sup> while the random structures were formed through the solid state dewetting<sup>31</sup> of 17 nm

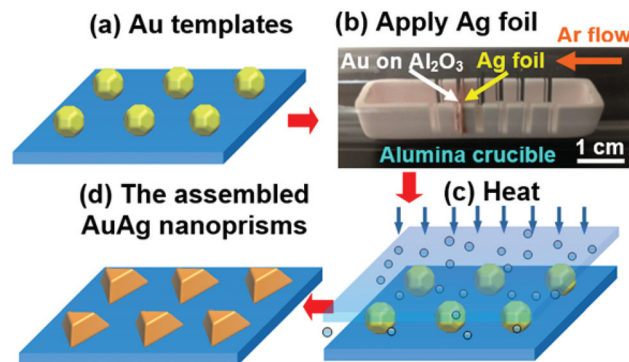


**Fig. 1** Schematic of the devised templated assembly process which transforms substrate-immobilized Au templates into triangular AuAg nanoprisms through the high temperature exposure of Au templates to a Ag flux derived from an adjacent foil. The image shows the experimental configuration utilized.

thick Au films. For both cases, the Au templates showed a high degree of epitaxy with the underlying substrate whereby the formation of [111]-oriented structures were favoured. The template-decorated substrate and a rectangular Ag foil of approximately the same dimensions were then inserted into slots cut into an alumina crucible (Fig. 1b). This configuration maintained a small well-defined distance (0.5 mm) between the two surfaces while preventing contact. The crucible was placed in a tube furnace with flowing Ar and heated to 775 °C, a temperature sufficient to drive a flux of Ag from the sublimating foil onto the adjacent substrate. Exposure of the Au templates to this flux resulted in the heterogeneous nucleation of Ag which leads to (i) a morphological transformation from the Wulff shape to a triangular nanoprism and (ii) a compositional transformation from pure Au to a AuAg alloy.

### Morphological characterization

Fig. 2a shows an SEM image of a periodic array of Au templates as well as top- and tilted-view images of the individual structures. The templates appear rounded, but where weak faceting is observed. The faceting is consistent with the equilibrium Wulff shape. Upon exposure to the Ag flux at elevated temperatures the array undergoes the transformation shown in Fig. 2b.

The individual structures now appear as triangular nanoprisms with the geometry expected for a structure enclosed by {111} facets. A close inspection of these structures, however, reveals that many of them exhibit a slight truncation of the prism corners by {100} facets. The nanoprisms form with two in-plane orientations differing by 180°, a common occurrence for [111]-oriented fcc metals<sup>37</sup> which originates from the fact that neither the ABCABC... nor the reverse ACBACB... stacking order is favoured through epitaxy. In addition to the nanoprisms there are a small number of other structures which show geometries consistent with non-[111]-oriented structures. Noteworthy, is that these structures also show pronounced

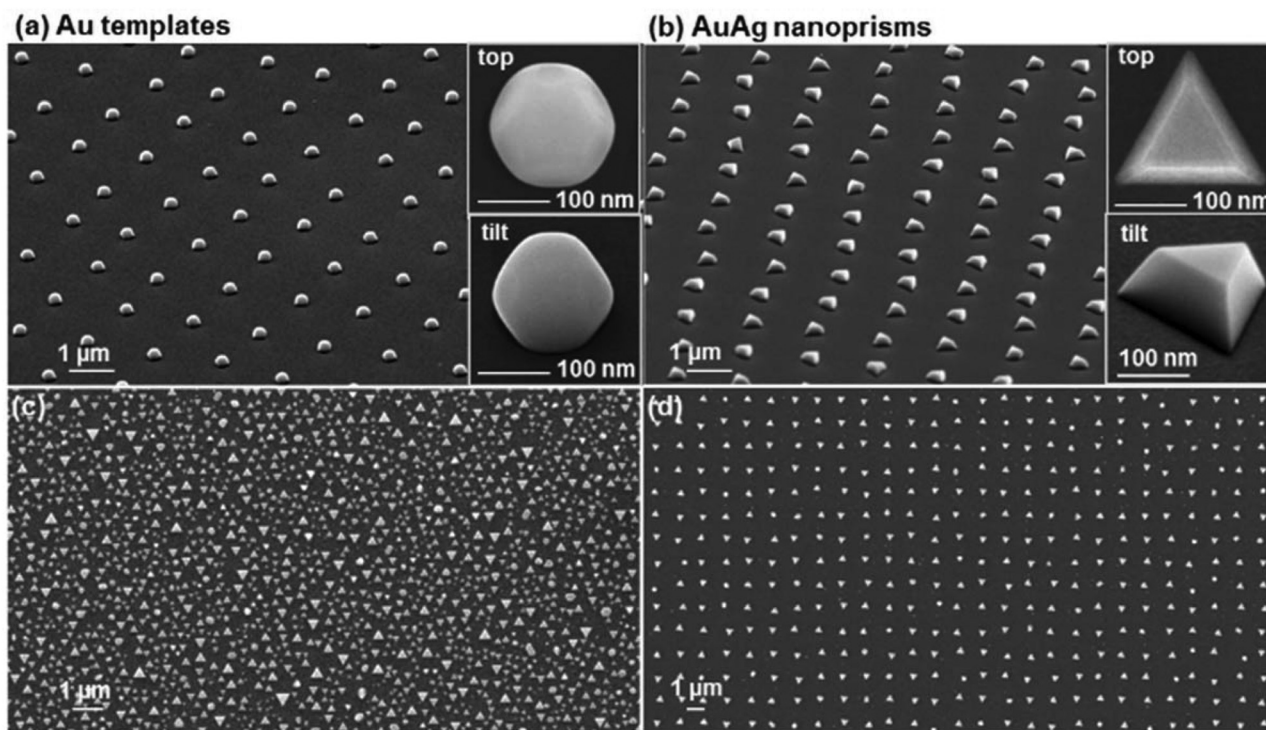


**Fig. 2** Tilted-view SEM images of a periodic array of (a) Au templates and (b) the AuAg nanoprisms derived from them. The insets show top- and 65° tilt-view images of the individual structures. Top-view images of the AuAg nanoprisms assembled using Au templates formed through the (c) solid state dewetting of an ultrathin Au film and (d) dynamic templating.

{111} faceting. When the same synthetic procedure is carried out on similarly shaped templates derived from the solid state dewetting of ultrathin Au films it yields a surface coated with triangular nanoprisms (Fig. 2c) where the randomness in the size and spacing of the initial Au templates is transcribed to the nanoprisms. For this scenario, there is a higher occurrence of structures which differ from the nanoprism geometry in that they are rounded, show substantial truncations and/or deviate from the preferred [111]-orientation. Nevertheless, significance is derived from the fact that a high yield of substrate-immobilized nanoprisms is obtained from templates which are easily fabricated over large areas.

Fig. 3 maps out the time-dependent evolution of the nanostructure morphology and composition which occurs as the Au template is transformed into a AuAg nanoprism. All of the structures shown experienced the identical processing conditions except for the exposure time to the Ag vapour at 775 °C which was varied from 30 to 600 min. At the beginning of the process the template is quite rounded, but where {100} and {111} faceting is apparent. The initial exposure of the templates to the Ag flux leads to the preferential growth on the {100} template facets (red arrows) and a sharpening of all edges where facets meet. The favoured growth on {100} facets ultimately leads to their annihilation. This occurs because each of these facets is bounded by four inward sloping {111} planes which reduce the area of a {100} facet with the addition of each successive layer until finally the

facet is extinguished by the pyramidal structure formed (green arrows). At this stage, which occurs after a 60 min exposure to the Ag flux, the emerging structure is bounded by eight {111} facets where seven of them are exposed and the eighth forms an interface with the substrate. Continued deposition on the remaining {111} facets leads to the annihilation of the three facets facing downwards towards the substrate as indicated by the yellow arrows. At this stage (90 min), nanoprism formation is complete. Longer deposition times lead to an increased height and edge length (600 min). Fig. 3b and c shows the time dependence of the nanostructure width and height, where the width plotted is the diameter for rounded particles and the edge length for nanoprisms. The width steadily increases, trending toward a constant value for long time intervals. The height of the structure first declines and then rises steadily. With the areal extent of the top facet diminishing due to three inward sloping {111} facets and the edge length of the overall structure trending toward a constant value, the rise in height is unsustainable. Instead, a steady-state configuration is expected whereby the amount of Ag arriving to the structure is equal to that which is desorbing from its surface. Consistent with this expectation is the evolution in nanostructure composition (Fig. 3d) obtained using EDS which initially shows rapid Ag alloying of the Au template followed by a more gradual increase in the Ag content which appears to be saturating at long time intervals. This data, combined with

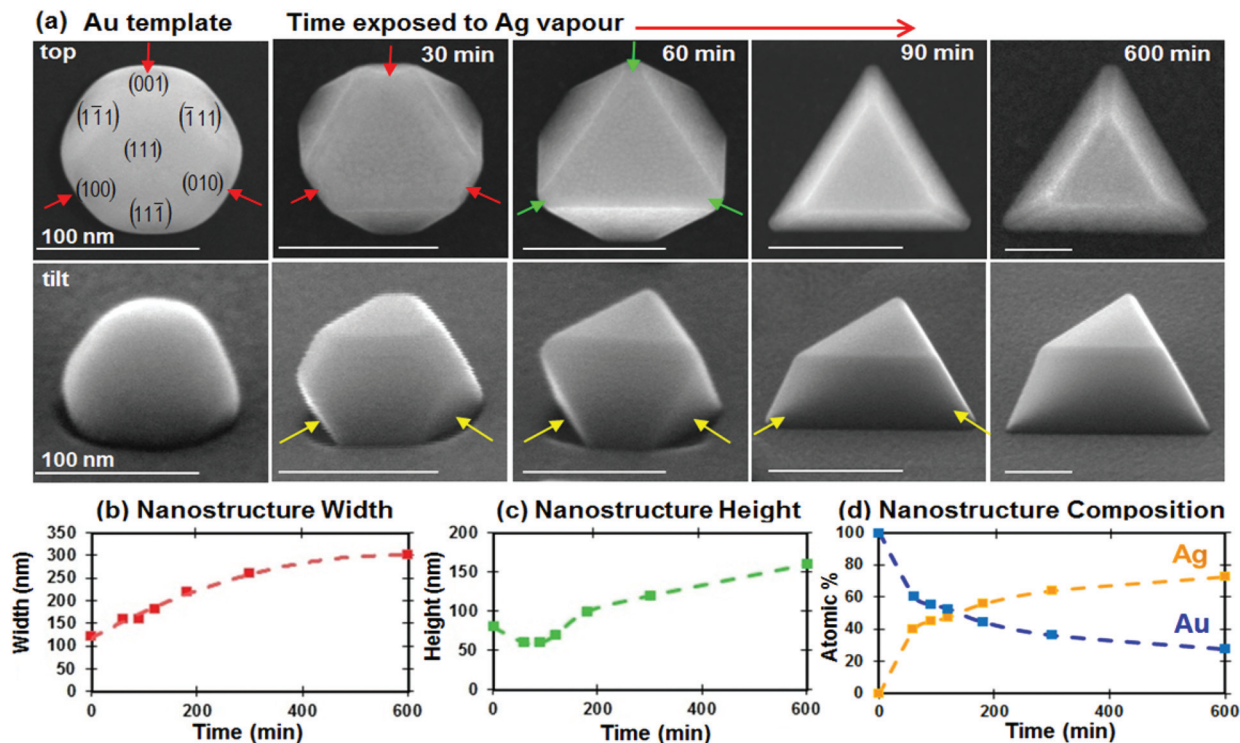


Fig. 3 (a) Top- and tilted-view SEM images showing a Au template with labelled facets and identical templates as they undergo a shape transformation resulting from their exposure to Ag vapour for time intervals extending from 30 to 600 min. Plots showing the temporal evolution of the nanostructure (b) width, (c) height and (d) composition.

estimates of the nanoparticle volume, indicate that the Au content within each structure remains approximately constant throughout the nanoprism assembly process.

### Crystal structure and compositional analysis

X-ray diffraction (XRD) and energy-dispersive X-ray spectroscopy (EDS) were used to characterize the crystallographic orientation and elemental homogeneity of the triangular nanoprisms. Because of the small lattice mismatch between Ag and Au ( $a_{\text{Ag}} = 4.0853 \text{ \AA}$ ,  $a_{\text{Au}} = 4.078 \text{ \AA}$ ) it was not possible to differentiate between pure Au and its Ag alloys. The  $\theta$ - $2\theta$  XRD scans do, however, reveal that both the Au templates and AuAg nanoprisms were, as expected, [111]-oriented (Fig. 4a). The intensity of the (111) reflection for the nanoprism sample is larger than that of the template due to the volume increase associated with the uptake of Ag. Elemental mapping and line-scans (Fig. 4b and c) strongly suggest that the nanoprisms are uniformly alloyed even though the images presented in Fig. 3 indicate that the deposition of Ag onto the template is highly anisotropic, suggesting considerable levels of interdiffusion between Au and Ag at the processing temperature. This is understandable both from the standpoint that the temperature is high enough to promote high levels of vacancy diffusion and the near ideal combination that Au and Ag present for promoting miscibility in the solid state as prescribed by the Hume-Rothery rules.

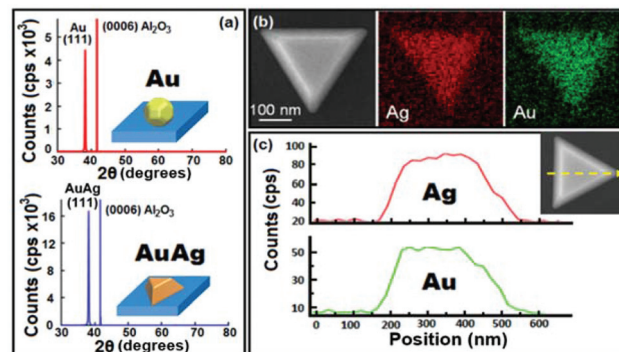
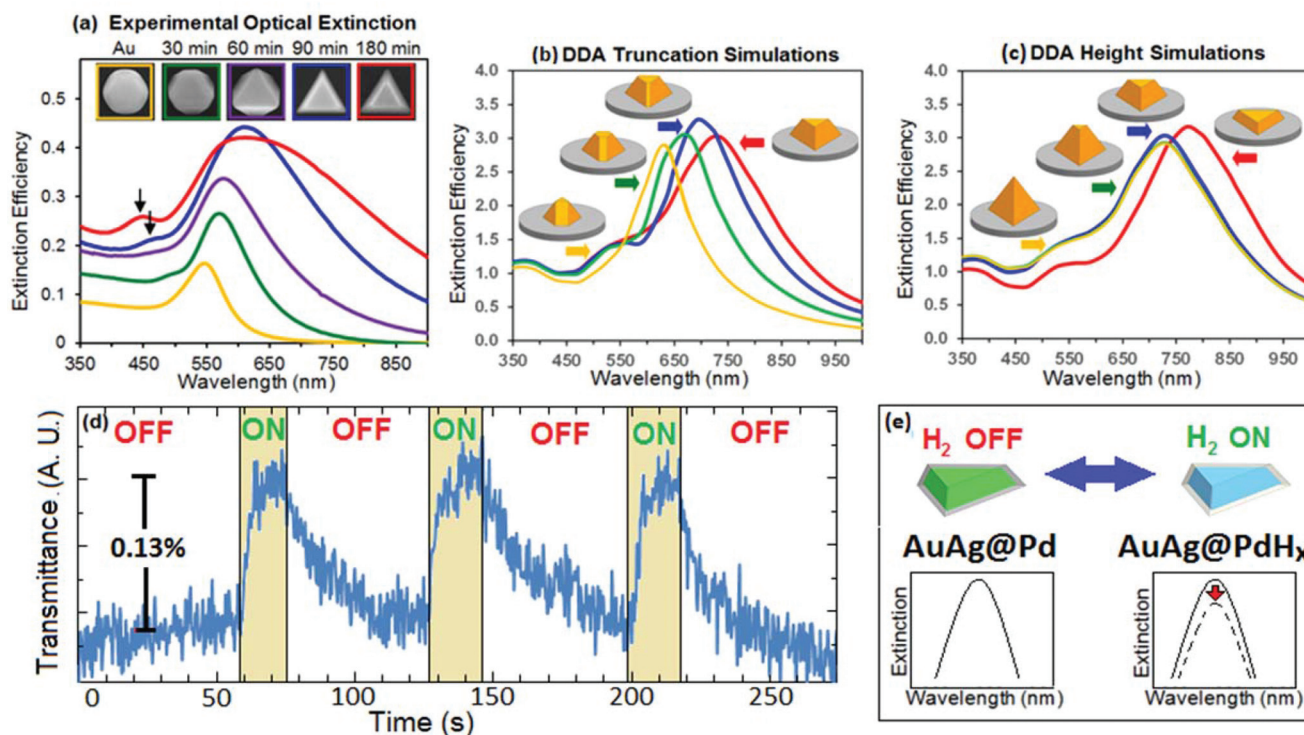


Fig. 4 (a)  $\theta$ - $2\theta$  XRD scans for the Au templates and the identical sample after the templates have been transformed into triangular AuAg nanoprisms. (b) SEM image of a nanoprism and the Ag and Au elemental maps derived from it. (c) Ag and Au elemental line-scans taken across the nanoprism as indicated by the yellow line in the inset.

### Optical properties and hydrogen sensing

Accompanying the morphological and compositional transformation from the Au template to a triangular AuAg nanoprism are dramatic changes to the optical properties. Fig. 5a shows the extinction spectra for a series of samples where nanoprism formation was halted at various stages. These measurements were carried out on structures formed in the random configuration due to the larger areas accessible for



**Fig. 5** (a) Optical extinction spectra for nanostructures which evolve from Au templates to triangular AuAg nanoprisms. DDA simulations of the extinction spectra where (b) the nanoprism corners are subjected to an increasing degree of truncation and (c) the height is systematically increased to the point where a tetrahedron is formed. (d) The integrated transmittance (476–731 nm) through an ensemble of Pd-coated AuAg nanoprisms exposed to on/off cycling of H<sub>2</sub> gas and (e) a schematic of the sensing mode responsible for H<sub>2</sub> detection.

characterization. SEM images of these samples are presented as ESI (Fig. S1†).

The LSPR red-shifts, broadens and increases in strength. In parallel, a quadrupole mode (black arrow) emerges and grows in strength as the nanoprisms become more well-defined. With the original template undergoing changes to its shape, volume and composition, the origins of the spectral dependency are somewhat convoluted. The results, however, can be rationalized using simulations based on the discrete dipole approximation (DDA)<sup>38</sup> and well-known experimental dependencies. The trend towards higher extinction as well as the red-shift and broadening of the LSPR are all consistent with a structure that is increasing in size. Also contributing to the red-shift and broadening of LSPR peak is the shape transformation from the Wulff shape to the nanoprism geometry.<sup>39</sup> Fig. 5b and c shows simulations of the extinction spectra for structures resting on a sapphire substrate where the degree of nanoprism truncation and height is systematically varied. They indicate that a substantial red-shift and a slight broadening is expected as the corners of the nanoprism sharpen while a blue-shift of a lesser degree originates from an increasing height. Also in agreement with the data is that nanoprism sharpening gives rise to a quadrupole mode at lower wavelengths ( $\lambda < 570$  nm).

These results are consistent with similar calculations carried out for freestanding nanoprisms.<sup>12,40</sup> The influence of

increasing levels of Ag on the optical response of the emerging nanostructure is also expected to be sizeable since Ag is known to dominate the optical response of AuAg alloys.<sup>41</sup> With pure Ag nanostructures having resonances which are narrower, more intense and blue-shifted relative to their Au counterparts,<sup>42</sup> increasing levels of Ag are responsible for the substantial increase in extinction and partial offset of the aforementioned LSPR red-shift and broadening caused by the shape transformation.

A single lithographically defined triangular nanoprism placed in close proximity to a nanoscale Pd disc has been demonstrated by Liu *et al.*<sup>9</sup> as an optical hydrogen sensor. The sensing mode is dependent on disruptions to the nanoprism's dielectric environment caused by the uptake of hydrogen by the palladium disc. Motivated by these findings we tested the hydrogen sensing capabilities of an ensemble of substrate-supported triangular nanoprisms coated with a 1 nm thick layer of Pd using a test apparatus and sensing strategy which we describe in detail elsewhere.<sup>8</sup> Briefly, the Pd coated AuAg nanoprisms (denoted as AuAg@Pd) are exposed to a broadband incoherent excitation (550–650 nm) resonant with the LSPR (*i.e.* the blue curve in Fig. 5a). The amount of transmitted light is then monitored as the sample is exposed to alternating on/off flows of 10% H<sub>2</sub> 90% N<sub>2</sub> gas. The transformation of the palladium to a metal hydride is expected to alter the dielectric environment of the AuAg nanoprism in a manner which

decreases the extinction and red-shifts the LSPR.<sup>43</sup> Fig. 5d and e shows the detection of hydrogen and a schematic illustrating the sensing mechanism. The observed cyclic behaviour is characterized by a rapid  $\sim 0.13\%$  rise in the integrated transmittance (476–731 nm) upon exposure to hydrogen followed by a gradual decline when the hydrogen flow is terminated. The rapid rise and gradual fall is a response characteristic of many metal hydride sensing modes where the hydrogen intake is more rapid than its loss.<sup>7</sup> Important is that neither the AuAg nanoprisms nor a standalone 1 nm thick Pd film yielded a comparable result, a clear indication that detection results from the coupled response originating from a metal hydride in intimate contact with a plasmonic nanoprism. By themselves the AuAg templates showed no well-defined response while the Pd film initially showed a small detectable response, but which, after several cycles, significantly degraded.

## Discussion

### Kinetically driven nucleation and growth

The experiments carried out demonstrate that the mere exposure of substrate-immobilized Au nanostructures to Ag adatoms at elevated temperatures results in their transformation to alloyed structures with altered geometries, but where the original heteroepitaxial relationship of the Au structure is preserved. Crucial to the assembly process is that the temperature is maintained in a regime where Ag adatoms are unable to cluster in sufficient numbers to nucleate a stable Ag nanostructure before desorbing from the substrate surface. Consequently, Ag adatoms are only able to remain on the substrate surface for extended periods of time if a suitable heterogeneous nucleation site is encountered. With a hierarchy of bond dissociation energies of Au–Au: 2.34 eV, Au–Ag: 2.10 eV, Ag–Ag: 1.68 eV,<sup>44</sup> the formation of Au–Ag bonds have the potential to significantly extend the adatom lifetime when compared to the Ag–Ag bonds needed to form pure Ag clusters on the substrate. The miscibility of the Au–Ag system then permits Ag vacancy diffusion into bulk Au where Ag atoms are completely stabilized against desorption until they randomly diffuse to the surface. Over time the structure increases in volume as more Ag adatoms are incorporated, but where this additive process is increasingly offset by the Ag desorption. Desorption rates are expected to increase due to the growing: (i) surface area of the alloyed structure, (ii) likelihood that bulk Ag will diffuse to the surface and (iii) reliance on the weaker Ag–Ag bonds within the structure. Eventually, the structure reaches a steady state configuration characterized by an equal number of Ag atoms arriving to and leaving the structure.

While the transformation of the Au nanostructures to a Au–Ag alloy is readily understood, the accompanying shape-transformation is far more subtle. Revealing is the fact that the dewetting process, when carried out using ultrathin AuAg films (Fig. S2†), gives rise to rounded structures with many showing faceting consistent with the Wulff shape. The result suggests that the Wulff shape remains the equilibrium con-

figuration for the AuAg alloy. We, therefore, assert that nanoprism formation is driven, not by the energy minimization of the overall structure, but by kinetic processes which favour the establishment of {111} facets. Strongly supportive of our assertion are the molecular dynamics (MD) simulations of Baletto *et al.*<sup>45</sup> which show that kinetic regimes exist where the arrival and attachment of Au or Ag adatoms to their respective Wulff configurations drive the geometry towards a {111} faceted octahedron. While their simulations pertain to homogeneous nucleation, many of their theoretical arguments can be extended to the heterogeneous case.

For the Au nanostructure to maintain its equilibrium Wulff shape, it would require the isotropic attachment of Ag adatoms to the various facets. Anisotropies are, however, inherent to our assembly process. Ag atoms which sublime from the foil can arrive to the Au nucleation site through direct impingement or by landing on the substrate and diffusing to its base. The latter process can lead to the preferential arrival of adatoms to those facets which intersect the substrate. Nanowire growth modes, for example, are often dominated by the arrival of adatoms at the nanowire base from what is termed as the collection area.<sup>46</sup> Further anisotropies originate from the unique bonding environment which the (100) and (111) facets present to a Ag adatom. Adatoms on the (100) surfaces are bonded to four nearest neighbour Au atoms while those on the close-packed (111) surface are bonded to only three. As a result of the higher coordination and stronger bonding, adatom surface diffusion on the (100) facets is slower<sup>45</sup> and desorption is less probable. Adatom diffusion between the various facets is also subject to kinetic disruptions. For such a transfer to occur, the adatom must first relinquish bonds on one facet and then reform them on another. Such a process inevitably leads to an energy barrier, the so-called Ehrlich–Schwoebel barrier,<sup>47,48</sup> with a barrier height dependent on the particular facets involved. Because these barriers tend to reflect adatoms,<sup>49</sup> they present obstacles of varying degrees to the surface diffusion of adatoms between various facets. Significant reductions to the barrier height can, however, occur through exchange processes whereby an adatom assumes the position of a surface atom located at the facet edge in a manner which causes this surface atom to be displaced and promoted to the adjacent facet. When such a process is repeated over and over it can result in a directional diffusion of adatoms from one facet type to another. Significant is the fact that MD simulations of these various processes by Baletto *et al.*<sup>45</sup> for the case of homogeneous nucleation reveal that it is relatively easy for adatoms to cross from a (111) to a (100) facet, but not *vice versa*. The result, therefore, provides the mechanism by which adatoms become preferentially trapped on {100} facets. With this understanding of the kinetic anisotropies inherent to the assembly process, we propose a mechanistic framework by which the transformation from a Au Wulff shape to a AuAg triangular nanoprism could occur. It is presented as a three stage process (Fig. 6), but where it should be understood that there is a significant overlap between the stages.

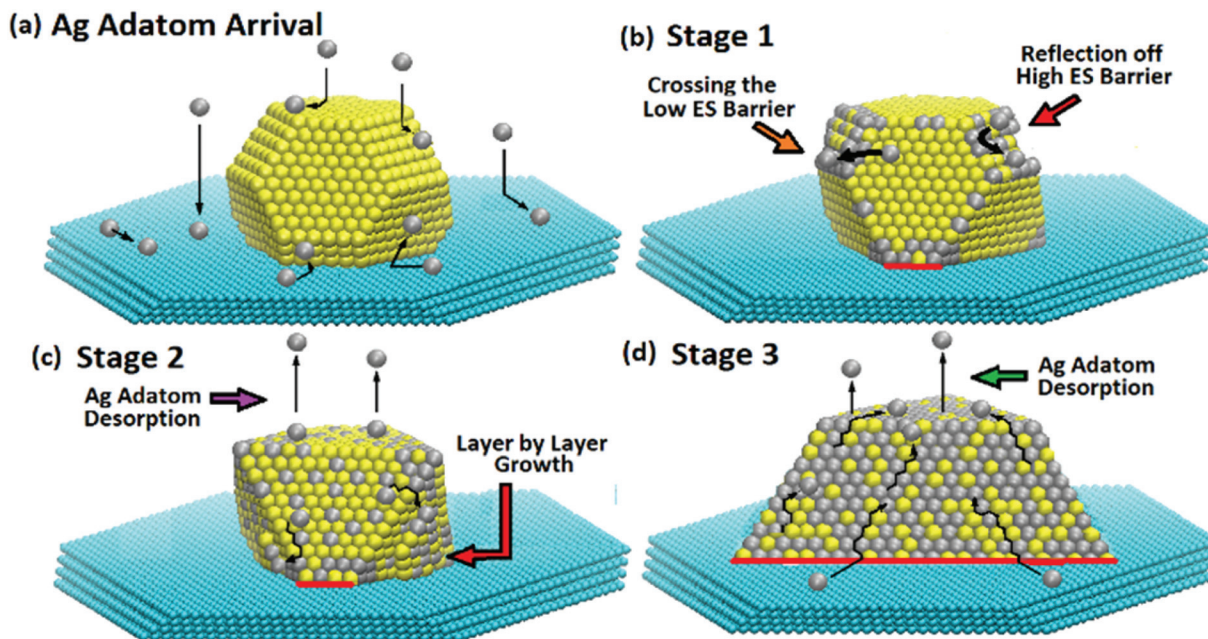


**Fig. 6** Schematic representation of the key elements which drive each of the three stages of the kinetically driven transformation of Wulff-shaped Au into triangular AuAg nanoprisms resulting from (a) the arrival of Ag adatoms to the template through direct impingement and surface diffusion. (b) Stage 1 processes where adatoms preferentially collect and deposit on  $\{100\}$  facets due to the varying Ehrlich–Schwoebel (ES) barriers. (c) Stage 2 processes where layer-by-layer growth is nucleated at the sites provided by the substrate–nanostructure interface where downward facing facets form and where Ag is increasingly desorbed from the top facet. (d) Stage 3 processes where adatoms arriving to the structure *via* substrate surface diffusion diffuse up the sidewalls and nucleate growth on the top facet.

In the first stage, Ag, which has arrived to the Au nucleation site, preferentially deposits on the high surface energy nucleation sites provided by the rounded regions and  $\{100\}$  facets (Fig. 6a). The rounded regions, which are characterized by step-terrace morphologies on atomic length-scales,<sup>51</sup> sharpen because they present excellent nucleation sites for growth since adatoms can simultaneously form bonds to both the step and terrace. There is then preferential surface diffusion from the  $\{111\}$  to  $\{100\}$  facets which leads to the accumulation of Ag atoms in sufficient number to induce layer-by-layer growth on all  $\{100\}$  facets (Fig. 6b). Such processes proceed at relatively high rates until growth on  $\{100\}$  results in the formation of faceted pyramids enclosed by  $\{111\}$  facets (Fig. 6c). Concurrent with these processes is the bulk intermixing of Au and Ag *via* vacancy diffusion.

The second stage is dominated by slow layer-by-layer growth on the downward facing  $\{111\}$  facets and an overall reduction in the height of the structure. With only  $\{111\}$  facets remaining, preferential growth on downward facing facets is facilitated by the higher flux of Ag adatoms arriving from the adjacent collection area. It is also possible that the high contact angle formed between these three facets and the substrate provides a nucleation site from which layer-by-layer growth is initiated. For the overall structure to lose height the top facet must be losing layers through the desorption of Ag at a rate greater than it is being replaced. At the end of this stage, the downward facing facets are filled in to complete the nanoprism geometry (Fig. 6c).

In the third stage, the nanoprism slowly gains height through layer-by-layer deposition on the top facet while the three side-facets grow, but at a much slower rate. This reversal from a gradual height loss to a gain is readily understood if the material required for this growth is being sourced from the collection area *via* the three remaining facets which are in contact with the substrate. At the beginning of the second stage the contact between these facets and the substrate is minimal (red line in Fig. 6c) and, as a result, they could not source enough material from the collection area to counter-balance the loss of Ag through desorption. It is noted that diffusion to the top facet *via* the downward facing facets is far less probable since these facets do not share an edge with the top facet and, as a result, surface diffusion from these facets to the top facet requires the adatom to cross a minimum of two Ehrlich–Schwoebel barriers. By the end of second stage, however, the line of contact between the remaining facets and the substrate has more than tripled (red line in Fig. 6d), and in doing so, provides the ability to source many more adatoms from the substrate. With all three of these side facets now supplying adatoms to the top facets it is able to grow in a layer-by-layer manner (Fig. 6d). This growth, however, is offset by increasing Ag desorption as the structure increases in surface area and volume. The structure, therefore, trends toward a steady-state configuration where the number of Ag atoms arriving to the structure is balanced by number exiting.

Thus far, the proposed mechanistic framework, as well as the MD simulations of Baletto *et al.*,<sup>45</sup> does not preclude the

possibility of transforming homogeneous nucleation sites of Ag into Ag nanoprisms. Attempts to achieve this outcome were only partially successful since Ag nanoprisms formed in low yield and many of the nucleation sites experienced a net volume loss (Fig. S3†). All of the nucleation sites able to support growth did, however, show a substantial sharpening of their facets. These results, hence, emphasize the important role which the far less volatile Au atoms play in stabilizing the nanoprism geometry.

## Conclusion

We have demonstrated a method for transforming Au nanoparticles shaped as truncated octahedrons into AuAg triangular nanoprisms which are substrate-immobilized, single-crystalline, epitaxially aligned and surfactant-free. In the devised route, Au nanoparticles serve as heterogeneous nucleation sites for Ag adatoms sourced from a sublimating foil. The observed transformation was unexpected because the nanoprism geometry does not represent the low surface energy configuration which typically transpires in high temperature assembly processes reliant on solid state diffusion. This deviation from the norm is attributed to the anisotropies in kinetic processes associated with (i) adatoms arriving preferentially to the base of nucleation site from an adjacent collection area, (ii) higher adatom diffusion rates on {111} facets than on {100} facets, and (iii) the various Ehrlich–Schwoebel barriers which inhibit adatom motion between facets. These anisotropies combined with the constant arrival, desorption and interdiffusion of Ag into Au at the nucleation site leads to the non-equilibrium steady state nanoprism geometry which, upon cooling, maintains this ‘frozen-in’ configuration. Obtained in high yield from a relatively simple procedure, the so-formed nanoprisms present the opportunity to form photonic surfaces for catalytic, sensing and photovoltaic applications. The optical properties of the nanostructures and the hydrogen sensing capabilities of Pd covered nanoprisms were also reported.

## Experimental section

### Nanoprism formation

Au templates were formed as both randomly positioned structures and as periodic arrays using assembly techniques described in detail elsewhere.<sup>36,50</sup> Briefly, the random structures were formed through the solid state dewetting of 17 nm thick Au films which were sputter deposited from Au targets with 99.9985% purity. The (0001)-oriented sapphire substrates, which had dimensions of 14 × 6 mm were cleaved from 3 in. diameter wafers. Templates formed as periodic arrays were derived from a directed-assembly process referred to as dynamic templating.<sup>50</sup> It uses a shadow mask with a periodic array of holes (diameter = 0.9 μm, pitch 1.6 μm) to define sacrificial Sb pedestals (*h* = 50 nm, 99.999% purity) upon which a 17 nm Au film is deposited. When heated, Sb sublimation results in a forced migration of the Au to the center of each

pedestal. At the end of the process the Sb has completely sublimed/evaporated, leaving behind a periodic array of substrate-immobilized Au nanostructures. Details regarding the characterization of these structures and the temperature regimens used for their assembly are reported in the earlier publications. The substrate and a 0.025 mm thick Ag foil (99.998% purity) with areal dimensions similar to those of the substrate were then placed into slots cut into an alumina crucible (Fig. 1b) such that the templates were facing the foil with a separation distance of 0.5 mm. The AuAg nanostructures were then formed by placing the crucible into a quartz tube furnace with flowing Ar (ultra high purity, flow = 65 sccm) and heated to 775 °C for the various durations reported. It is noted that a dedicated quartz tube was used for each of the steps described in order to prevent cross-contamination.

### Instrumentation

Au and Sb depositions utilized a Model 681 Gatan High Resolution Ion Beam Coater. The assembly processes were carried out in a Lindberg Blue M tube furnace. SEM images and EDS measurements were obtained using a FEI Quanta 450 FEG SEM Environmental Scanning Electron Microscope operating in secondary electron mode. The samples were coated with a conducting Au<sub>0.5</sub>Pd<sub>0.5</sub> layer to enhance image quality. The extinction spectra were obtained using a Jasco UV/Vis Spectrophotometer V650. X-ray diffraction measurements utilized a Bruker D8 Discover X-ray diffractometer. The instrumentation used for hydrogen detection is described elsewhere.<sup>8</sup>

### Discrete dipole approximation simulations

DDA calculations of the extinction efficiency were carried out using DDSCAT (Version 7.3)<sup>39</sup> where the simulated structures were first created using LAMMPS.<sup>52</sup> The simulated nanoprism, Fig. 5b, (edge length = 150 nm, height = 60 nm, {111} facets) and underlying substrate (diameter = 250 nm, height = 20 nm) were defined collectively by 40 730 dipoles. The subsequent truncations of this nanoprism revealed {100} facets with widths of 11, 23 and 38 nm. The edge length of the simulated nanoprism in Fig. 5c was held constant while the height was varied between four values (30, 60, 90 and 122 nm). The dielectric constants for a Au<sub>0.5</sub>Ag<sub>0.5</sub> alloy<sup>53</sup> were used for the nanostructure while values for sapphire were obtained from Palik.<sup>54</sup> The *k*-vector of the incident photon was normal to the substrate surface while its oscillating E-field was directed toward a corner of the nanoprism. The schematics in Fig. 6 were coded in LAMMPS and visualized using Visual Molecular Dynamics (VMD).<sup>55</sup>

## Acknowledgements

This work is funded by the NSF (DMR-1053416) CAREER Award to S. Neretina. The authors also acknowledge the expertise of D. Dikin (Facility Manager, Nano Instrumentation Center, Temple University). The work has benefited from the facilities available through Temple University's Material Research Facility (MRF). D. Sil acknowledges support

provided by the Army Research Laboratory through contract W911NF-10-2-009. K. D. G. acknowledges support received through a Temple University Graduate Student Fellowship.

## Notes and references

- G. Baffou and R. Quidant, *Chem. Soc. Rev.*, 2014, **43**, 3898.
- M. Xiao, R. Jiang, F. Wang, C. Fang, J. Wang and J. C. Yu, *J. Mater. Chem. A*, 2013, **1**, 5790.
- C. Clavero, *Nat. Photonics*, 2014, **8**, 95.
- S. Mubeen, J. Lee, W. Lee, N. Singh, G. D. Stucky and M. Moskovits, *ACS Nano*, 2014, **8**, 6066.
- Y. T. Tian and T. Tatsuma, *J. Am. Chem. Soc.*, 2005, **127**, 7632.
- Y. Takahashi and T. Tatsuma, *Appl. Phys. Lett.*, 2011, **99**, 182110.
- C. C. Wadell, S. Syreova and C. Langhammer, *ACS Nano*, 2014, **8**, 11925.
- D. Sil, K. D. Gilroy, A. Niaux, A. Boulesbaa, S. Neretina and E. Borguet, *ACS Nano*, 2014, **8**, 7755.
- N. Liu, M. L. Tang, M. Hentschel, H. Giessen and A. P. Alivisatos, *Nat. Mater.*, 2011, **10**, 631.
- M. W. Knight, Y. Wang, A. S. Urban, B. Y. Zheng, P. Nordlander and N. J. Halas, *Nano Lett.*, 2013, **13**, 1687.
- H. J. Chen, L. Shao, Q. Li and J. F. Wang, *Chem. Soc. Rev.*, 2013, **42**, 2679.
- J. E. Millstone, S. J. Hurst, G. S. Métraux, J. I. Cutler and C. A. Mirkin, *Small*, 2009, **5**, 646.
- K. L. Shuford, M. A. Ratner and G. C. Schatz, *J. Chem. Phys.*, 2005, **123**, 114713.
- S. Kim, J. Jin, Y.-J. Kim, I.-Y. Park, Y. Kim and S.-W. Kim, *Nature*, 2008, **453**, 757.
- M. M. Shahjamali, M. Bosman, S. Cao, X. Huang, X. Cao, H. Zhang, S. S. Pramana and C. Xue, *Small*, 2013, **9**, 2880.
- Y. Yang, X.-L. Zhong, Q. Zhang, L. G. Blackstad, Z.-W. Fu, Z.-L. Zhong, Q. Zhang, L. G. Blackstad, Z.-W. Fu, Z.-Y. Li and D. Qin, *Small*, 2014, **10**, 1430.
- R. Jin, Y. Cao, C. A. Mirkin, K. L. Kelly, G. C. Schatz and J. G. Zheng, *Science*, 2001, **294**, 1901.
- L. Scarabelli, M. Coronado-Puchau, J. J. Giner-Casares, J. Langer and L. M. Liz-Marzan, *ACS Nano*, 2014, **8**, 5833.
- X. Liu, L. Li, Y. Yang, Y. Yin and C. Gao, *Nanoscale*, 2014, **6**, 4513.
- Y. Huang, A. R. Ferhan, Y. Gao, A. Dandapat and D.-H. Kim, *Nanoscale*, 2014, **6**, 6496.
- C. Xue, Z. Li and C. A. Mirkin, *Small*, 2005, **1**, 513.
- A. Gopinath, S. V. Boriskina, B. M. Reinhard and L. Dal Negro, *Opt. Express*, 2009, **17**, 3741.
- C. L. Haynes and R. P. Van Duyne, *J. Phys. Chem.*, 2001, **105**, 5599.
- B. Cui, L. Clime, K. Li and T. Veres, *Nanotechnology*, 2008, **19**, 145302.
- S. Viarbitskaya, A. Teulle, R. Marty, J. Sharma, C. Girard, A. Arbouet and E. Dujardin, *Nat. Mater.*, 2013, **12**, 426.
- J.-S. Huang, V. Callegari, P. Geisler, C. Brüning, J. Kern, J. C. Prangma, X. F. Wu, T. Feichter, J. Ziegler, P. Weinmann, M. Kamp, A. Forchel, P. Biagioni, U. Sennhauser and B. Hecht, *Nat. Commun.*, 2010, **1**, 150.
- Y. Zhou, X. Zhou, D. J. Park, K. Torabi, K. A. Brown, M. R. Jones, C. Zhang, G. C. Schatz and C. A. Mirkin, *Nano Lett.*, 2014, **14**, 2157.
- D. Li, C. Wang, D. Tripkovic, S. Sun, N. M. Markovic and V. R. Stamenkovic, *ACS Catal.*, 2012, **2**, 1358.
- Z. Niu and Y. Li, *Chem. Mater.*, 2014, **26**, 72.
- M. S. J. Marshall and M. R. Castell, *Chem. Soc. Rev.*, 2014, **43**, 2226.
- C. V. Thompson, *Annu. Rev. Mater. Sci.*, 2012, **42**, 399.
- C. R. Henry, *Prog. Surf. Sci.*, 2005, **3–4**, 92.
- A. Sundar, P. Farzinpour, K. D. Gilroy, T. Tan, R. A. Hughes and S. Neretina, *Small*, 2014, **10**, 3379.
- A. Sundar, P. Farzinpour, K. D. Gilroy, T. Tan, R. A. Hughes and S. Neretina, *Cryst. Growth Des.*, 2013, **13**, 3847.
- A. Sundar, R. A. Hughes, P. Farzinpour, K. D. Gilroy, G. A. Devenyi, J. S. Preston and S. Neretina, *Appl. Phys. Lett.*, 2012, **100**, 013111.
- P. Farzinpour, A. Sundar, K. D. Gilroy, Z. E. Eskin, R. A. Hughes and S. Neretina, *Nanoscale*, 2013, **5**, 1929.
- H. Bialas and K. Heneka, *Vacuum*, 1994, **45**, 79.
- B. T. Draine and P. J. Flatau, *J. Opt. Soc. Am. A*, 1994, **11**, 1491.
- B. T. Draine and P. J. Flatau, User Guide to the Discrete Dipole Approximation Code DDSCAT 7.2, <http://arXiv.org/abs/1202.3424>, 2012.
- K. L. Kelly, E. Coronado, L. L. Zhao and G. C. Schatz, *J. Phys. Chem. B*, 2003, **107**, 668.
- S. Link, Z. L. Wang and M. A. El-Sayed, *J. Phys. Chem. B*, 1999, **103**, 3529.
- M. Rycenga, C. M. Cobley, J. Zeng, W. Y. Li, C. H. Moran, Q. Zhang, D. Qin and Y. N. Xia, *Chem. Rev.*, 2011, **111**, 3669.
- S. Syreova, C. Wadell and C. Langhammer, *Nano Lett.*, 2014, **14**, 2655.
- Y. R. Luo, *Comprehensive Handbook of Chemical Bond Energies*, CRC Press, Boca Raton, Florida, 2007, pp. 9–65.
- F. Baletto, C. Mottet and R. Ferrando, *Surf. Sci.*, 2000, **446**, 31.
- M. C. Plante and R. R. Lapierre, *J. Cryst. Growth*, 2006, **286**, 394.
- J. J. de Miguel and R. Miranda, *J. Phys.: Condens. Matter*, 2002, **14**, R1063.
- S. J. Liu, H. Huang and C. H. Woo, *Appl. Phys. Lett.*, 2002, **80**, 3295.
- G. L. Kellogg, *Surf. Sci. Rep.*, 1994, **21**, 1.
- P. Farzinpour, A. Sundar, K. D. Gilroy, Z. E. Eskin, R. A. Hughes and S. Neretina, *Nanotechnology*, 2012, **23**, 495604.
- H. Ohnishi, Y. Kondo and K. Takayanagi, *Surf. Sci.*, 1998, **415**, L1061.
- S. Plimpton, *J. Comput. Phys.*, 1995, **117**, 1 <http://lammps.sandia.gov>.
- Y. Nishijima and S. Akiyama, *Opt. Mater. Express*, 2012, **2**, 1226.
- E. D. Palik, *Handbook of Optical Constants of Solids*, Academic Press, New York, NY, 1998.
- W. Humphrey, A. Dalke and K. Schulten, *J. Mol. Graphics*, 1996, **14**, 33.